ARTICLE

Check for updates

# Stress relaxation arrested the mainshock rupture of the 2016 Central Tottori earthquake

Yoshihisa Iio [1] ✉, Satoshi Matsumoto[2], Yusuke Yamashita[1], Shin'ichi Sakai[3], Kazuhide Tomisaka[1], Masayo Sawada[1], Takashi Iidaka[3], Takaya Iwasaki[3], Megumi Kamizono[2], Hiroshi Katao[1], Aitaro Kato [3], Eiji Kurashimo[3], Yoshiko Teguri[4], Hiroo Tsuda[5] & Takashi Ueno[4]

After a large earthquake, many small earthquakes, called aftershocks, ensue. Additional large earthquakes typically do not occur, despite the fact that the large static stress near the edges of the fault is expected to trigger further large earthquakes at these locations. Here we analyse ~10,000 highly accurate focal mechanism solutions of aftershocks of the 2016 Mw 6.2 Central Tottori earthquake in Japan. We determine the location of the horizontal edges of the mainshock fault relative to the aftershock hypocentres, with an accuracy of approximately 200 m. We find that aftershocks rarely occur near the horizontal edges and extensions of the fault. We propose that the mainshock rupture was arrested within areas characterised by substantial stress relaxation prior to the main earthquake. This stress relaxation along fault edges could explain why mainshocks are rarely followed by further large earthquakes.

[1] Disaster Prevention Research Institute, Kyoto University, Gokasho Uji, Japan. [2] Institute of Seismology and Volcanology, Faculty of Sciences, Kyushu University, Fukuoka, Japan. [3] Earthquake Research Institute, University of Tokyo, Tokyo, Japan. [4] Japan Meteorological Agency, Tokyo, Japan. [5] Ministry of Education, Culture, Sports, Science and Technology, Tokyo, Japan. ✉email: iio@rcep.dpri.kyoto-u.ac.jp

Following a large earthquake, shear stress increases along the edges and extensions of the fault where the slip of the earthquake did not occur[1]. This stress is added to the stress that accumulated before the earthquake; thus, if the fault and its surroundings were in a state of uniform stress before the earthquake, it is thought that the fault edges and extensions would subsequently be in a very unstable state, allowing earthquakes to be easily generated[2]. This is demonstrated in Fig. 1a, in which the stress profile along the fault strike is shown for a vertical strike-slip fault with a simplified slip model (see "Methods"). It is assumed that the same amount of shear stress as the averaged stress drop on the mainshock fault is applied uniformly on the fault, inside and outside the mainshock rupture area during an interseismic period. This stress level is thought to indicate the apparent strength of the fault, since the mainshock occurs when the shear stress increases to this level. If the strength is assumed to be uniform on the fault and its extension, it is clear that the stress after the mainshock becomes greater than the strength near the edges of its rupture area and beyond. Thus, large earthquakes will be generated there. However, in intraplate regions, large earthquakes are rarely followed by other large earthquakes in adjacent areas; typically, only smaller earthquakes occur and, then, decrease in frequency roughly with the reciprocal of time after the mainshock. However, occasionally seismic sequences are characterised by the occurrence of multiple large earthquakes[3–5], and

forecasting such phenomena remains a major issue in seismology[3]. At present, the cause of seismic activity following large earthquakes is controversial and includes static[6–8] and dynamic triggers[9–11] as well as the effect of pore fluid pressure[12], and no clear physical model has been established to date. Therefore, aftershocks are forecasted statistically[13], and it has been reported that aftershock activity is sometimes unusual before other large earthquakes[3].

The question of whether or not a subsequent major earthquake will occur along the edges and extensions of a mainshock fault is compounded by the questions of why rupture propagation of a large earthquake stops at its edge and how the size of the earthquake is determined[14,15]. When rupture propagation stops at an ordinary high-strength barrier, it may be possible for a large event to occur[16]. On the contrary, in the case of low strength and/or low-stress barriers, such as volcanos[16–19], this may not be common. Ke et al.[19] emphasised the importance of the low-stress barrier called the earthquake arrest zone, using laboratory experiments and dynamic rupture simulations. Endpoints of earthquake faults, large bends[20], offsets[21], or damage zones, such as horsetail splays or branch faults[22], are recognised from the surface traces of active faults. However, a systematic study of strike-slip fault surface traces showed that at one endpoint of nearly half of all faults analysed, the reason for the cessation of rupture is unknown[23]. Moreover, the stress
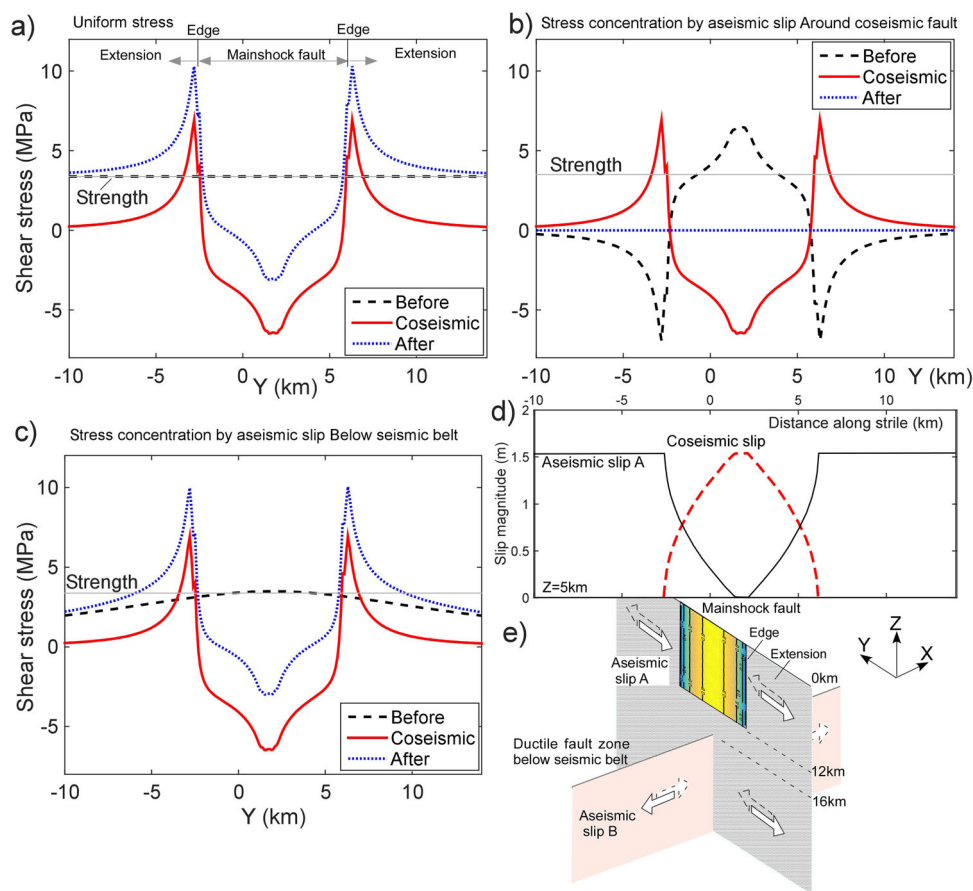

Fig. 1 Stress profile along the fault strike for a vertical strike-slip fault. a Uniform stress case. The shear stress on the mainshock fault, at the edge, and in the extension before and after the mainshock shown by the black dashed, and blue dotted lines, respectively. The coseismic change is shown by a red line. The apparent strength of the fault is shown by a grey line. **b** Case of stress concentration by the aseismic slip around the mainshock fault. The aseismic slip (A) mainly occurred on the fault shown by grey in Fig. 1e. **c** Case of stress concentration by the aseismic slip below the seismic belt[38]. The aseismic slip (B) occurred in the ductile fault zone below the seismic belt shown by pink in Fig. 1e. **d** Slip profiles of the coseismic slip and the aseismic slip around the mainshock fault for the case (**b**). **e** Geometries of the mainshock fault and the surrounding aseismic fault, and the ductile fault below the seismic belt. The slip distribution of the mainshock fault is shown by colour contours.
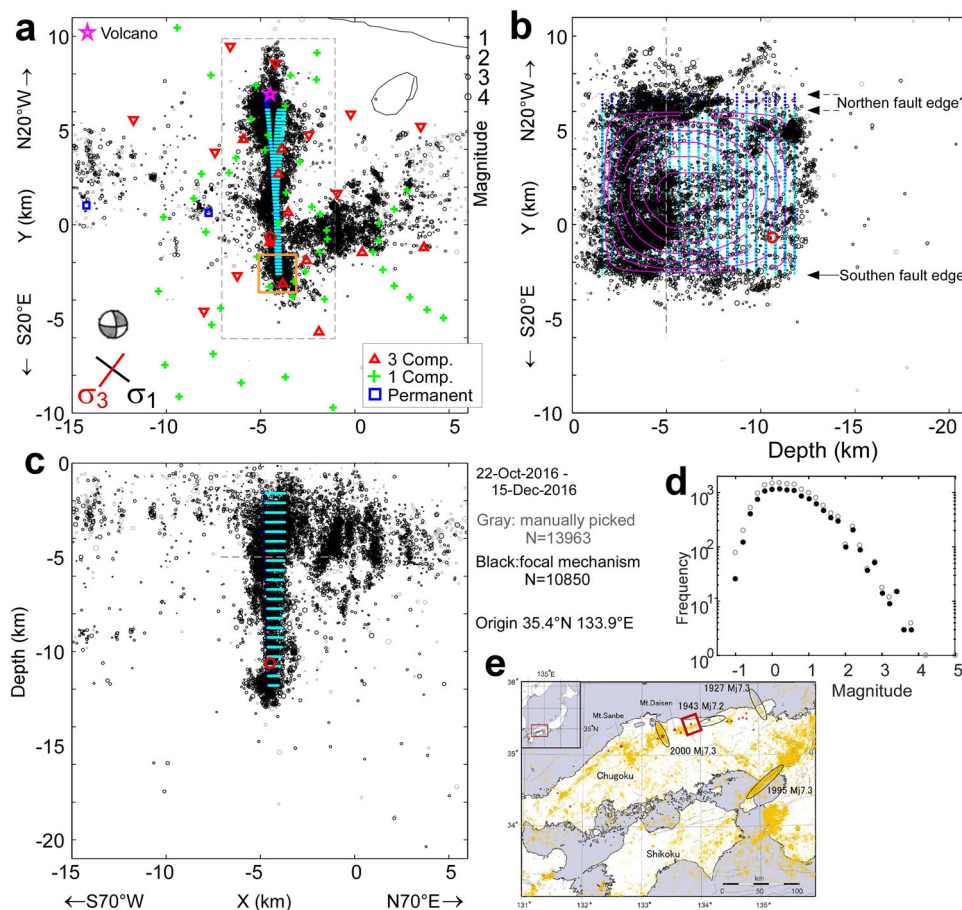
Fig. 2 Distribution of hypocentres and aftershock observation stations. a Plan view. Black circles are aftershocks that occurred from October 22 to December 15, 2016, for which focal mechanisms were determined. Grey circles were aftershocks that were manually picked. Locations of temporary seismic stations for one- and three-component seismographs and permanent stations (operated by the National Research Institute for Earth Science and Disaster Mitigation, NIED, and the Japan Meteorological Agency, JMA) are indicated by red triangles, green crosses, and dark blue rectangles, respectively. The cyan dots indicate the estimated mainshock fault. The possible locations of the northern edges of the WF are indicated by blue dots from $Y = 6.1$ to 6.9 km. The orange star indicates a quaternary volcano[39]. The focal mechanism (in the lower hemisphere) of the mainshock determined by JMA is shown by a grey and white beach ball[26]. The mean directions of σ_1 and σ_3 in this area, estimated from stress inversion analyses, are shown by black and red lines, respectively. The grey dashed rectangle indicates the area for which detailed analyses were performed. The orange square indicates the areas around the southern edge of the mainshock fault shown in Fig. 4. **b** Cross-section along the fault strike. The purple contours are the estimated slip distribution in 0.2 m increments, that overlap those of EF and WF (the case of the northern end of $Y = 6.1$). The red circle indicates the mainshock hypocentre determined by JMA. **c** Cross-section perpendicular to the fault strike. **d** Magnitude−frequency distributions of the aftershocks focal mechanisms of which were determined (black dots) and manually picked (grey circles). **e** Large scale map showing the aftershock region modified from Fig. 1 of Kawanishi et al.[25].

state at the edge of earthquake faults has yet to be estimated from observations.

Results and discussion

Estimation of the true mainshock fault plane and its horizontal edges. In this study, we estimated the stress state at the horizontal fault edges of a simple, moderately sized, strike-slip intraplate earthquake by precisely estimating the locations of the fault plane of the mainshock, including their horizontal edges, with an accuracy of ~200 m, from approximately 10,000 accurate focal mechanism solutions (see "Methods"). These solutions were determined from the data of both 44 permanent stations and 69 temporary seismic stations installed immediately after the occurrence of the 2016 Central Tottori earthquake ($Mw6.2$)[24] that occurred in the seismic zone near the coast of the Sea of Japan in the San'in district[25]. The distributions of the earthquake's aftershocks and seismic stations, and examples of focal mechanism solutions are shown in Fig. 2 and Supplementary Fig. 1, respectively. A foreshock of magnitude 4.2 occurred about 2 h before

the mainshock at almost the same location, as the mainshock and small earthquakes continued[26].

In recent years, it has become clear that many aftershocks occur outside the fault planes of mainshocks[27,28]. The changes in stress around the edges of faults caused by the mainshocks are tensional on one side and compressional on the other. Furthermore, the direction of the maximum compressive stress generated by the mainshocks is rotated 90°, with the fault as a boundary. It has previously been reported that aftershock focal mechanism solutions are in consistent with the 90° rotation[29]. For the 2016 Central Tottori earthquake, it was confirmed that nearly all aftershocks occurred outside the fault plane, since the orientations of the tension (T) axis of the optimal focal mechanism solutions for the Central Tottori earthquake vary by 20–40° near the fault around the southern edge, as shown in Fig. 3a. Similar off-fault aftershocks were detected for the 2000 Western Tottori Prefecture earthquake, and it is estimated from precise aftershock distributions that they occurred outside the damage zone[28]. It is also shown in Fig. 3a that with respect to the
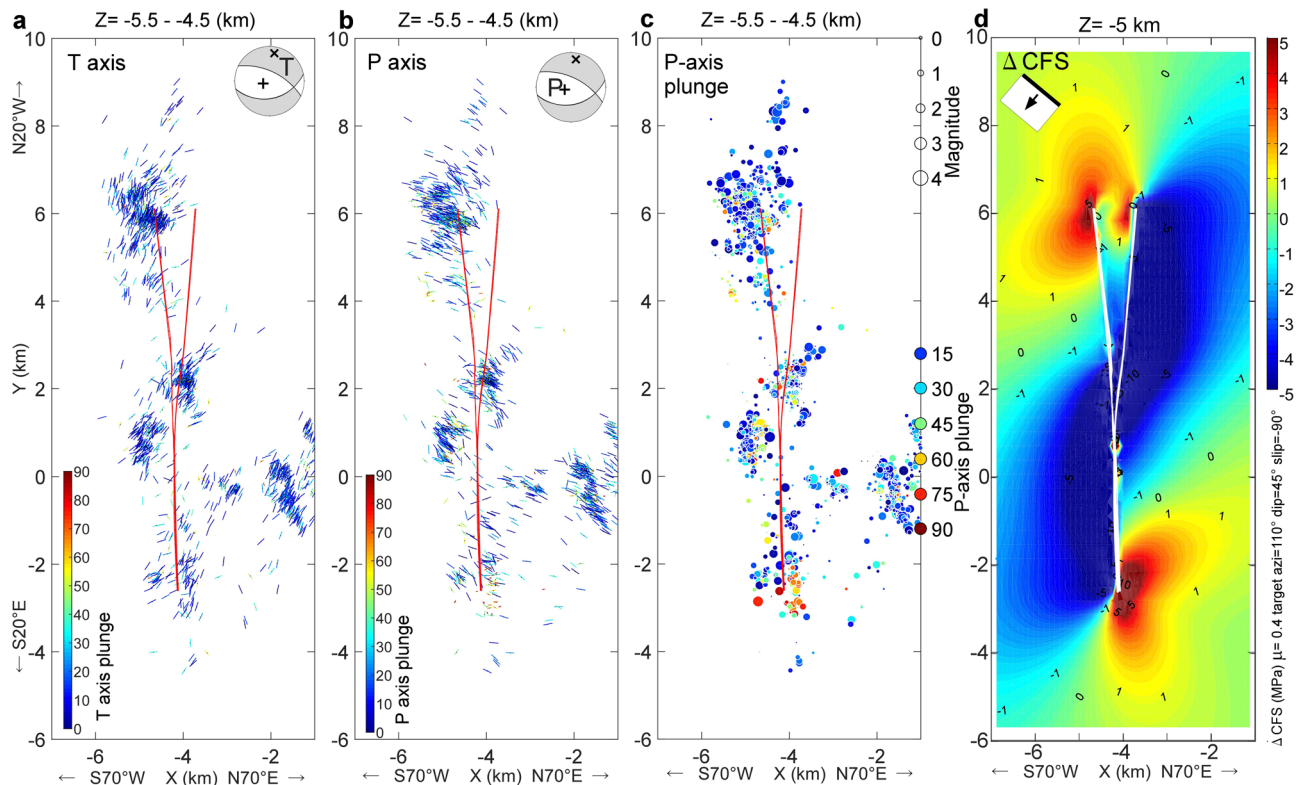
Fig. 3 Distributions of *T* and *P* axes and *P* axis plunge of optimal focal mechanism solutions and ΔCFS. a *T* (tension) axes of aftershocks located at depths of 5 ± 0.5 km projected onto the horizontal plane. Their plunges (i.e., angles measured from the horizontal) are indicated by colours from blue to red. The inset figure indicates the *T* axis on a focal mechanism solution. **b** *P* (pressure) axes. **c** *P* axis plunges; showing that normal faulting events have larger plunges. **d** Distributions of ΔCFS for normal faulting aftershocks with a fault strike of N110°E, a plunge of 45°, and a slip direction of −90°. The grey and white beach balls of focal mechanism solutions indicate the orientations of *T* and *P* axes in (**a**) and (**b**). The inset rectangle in (**d**) indicates the fault plane on which ΔCFS is calculated. The upper edge and slip direction are shown by the bold line and arrow. Red and white lines indicate the estimated fault planes at this depth. The northern edge of the WF was set at *Y* = 6.1 km in this figure.

pressure (*P*) axes, those with small plunges show similar differences. These are results from a depth of 5 ± 0.5 km, but similar results are seen at other depths, as shown in Supplementary Fig. 2. The locations of the mainshock fault planes and their horizontal edges were estimated from focal mechanism solutions and GNSS data[30] (see "Methods"). In the northern part, the fault planes are complicated and were estimated to be separated into two, the western fault (WF) and the eastern fault (EF), as shown in Fig. 3. Thus, the results obtained in the southern part are mainly discussed in this paper. However, similar shifts of T and P axes were observed around the northern edge of the WF.

It is worth noting that normal faulting aftershocks were concentrated on the eastern side of the southern fault edge, namely in the tensional region (Fig. 3c). The regions around the fault edges where the normal faulting aftershocks were concentrated matched well with the distribution of changes in the Coulomb failure stress (ΔCFS) for a normal fault calculated from the slip distribution of the mainshock, as shown in Fig. 3d.

Since normal faulting aftershocks are considered to be more easily triggered where the ΔCFS is large[31], we assumed that horizontal fault edges were located at the positions where the spatial average of the ΔCFS value for the normal faulting aftershocks was at maximum, and estimated the locations of the edges, as shown in Supplementary Figs. 3 and 4 (see "Methods").

A lot of aftershocks occurred around the fault edges, due to the stress concentration. In contrast, aftershocks also occurred in the central part, where the ΔCFS values were small for both strike-slip and normal faulting aftershocks. It is difficult to explain this by using a simple fault model as that employed in this study. The

source model inferred from strong-motion waveforms has two large slip regions in the northern and southern parts[32], and this model can explain those aftershocks. The purpose of this study is to investigate the properties of the horizontal fault edges, and the GNSS data used in this study do not have a resolution high enough for solving such a small region[30], therefore, this problem requires further research.

Stress state near the fault edge. Figure 4 shows the distribution of the *P* axis plunges of the aftershocks near the estimated southern fault edge at depths of 5 ± 0.5 km, together with ΔCFS for normal (Fig. 4a) and strike-slip (Fig. 4b) faulting aftershocks. These are results from a depth of 5 km, while those from all the depths are shown in Supplementary Figs. 5 and 6. The normal faulting aftershocks were notably concentrated in the region where the ΔCFS for the normal fault was larger. Meanwhile, in the region where the ΔCFS for the strike-slip fault with the same focal mechanism solution as the mainshock was larger, there were almost no strike-slip faulting aftershocks, which are denoted by blue colours. The strike-slip faulting aftershocks also appear to avoid the large ΔCFS region. At other depths in the southern part, a concentration of normal faulting aftershocks was observed, in particular at depths of 4 and 6 km, and strike-slip faulting aftershocks are absent, except at ~8 km (Supplementary Fig. 5).

The ΔCFS values in this study were calculated for stress changes due to the mainshock. It is known that before the mainshock, the stress field in this district was prone to strike-slip faulting earthquakes[25,29] (Fig. 2). If this stress field was spatially
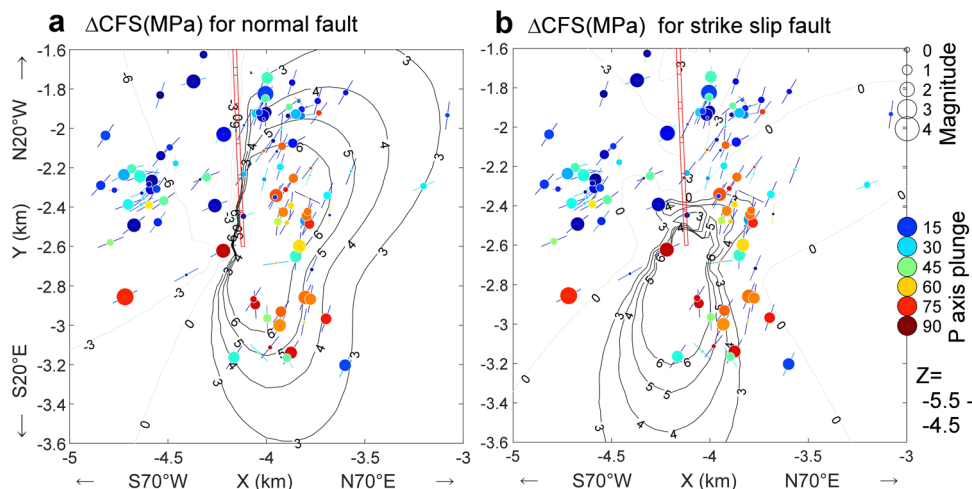
Fig. 4 Distributions of _P_ axis plunges, _T_ axes, and ΔCFS around the southern edge. a Filled circles indicate the _P_ axis plunges of aftershocks occurring within a $2 \times 2 \times 1\,km^3$ volume centred at the estimated fault edge at the depth of 5 km. Normal faulting aftershocks are characterised by _P_ axis plunges greater than 60°. _T_ axes are also projected onto the horizontal plane. ΔCFS are denoted for normal faulting aftershocks with a fault strike of N110°E, a plunge of 45°, and a slip direction of −90° with black contours of 3, 4, 5, and 6 MPa and grey contours of 0, −3, and −6 MPa. **b** ΔCFS for the same strike-slip fault as the mainshock. The other items in the figure are the same as for (**a**). The red line indicates the estimated fault plane at the depth of 5 km.

uniform, the total shear stress after the mainshock (expressed as the sum of the stress field before the mainshock and the change in stress due to the mainshock) would be expected to greatly increase along the fault edge. Many historical, large earthquakes in this area[25] have suggested that the stress state is critical (i.e., close to failure). If the stress concentration along the fault edge is further added to this critical uniform stress field, it is expected to be extremely prone to earthquakes; however, at least during the four years after the mainshock, no larger earthquakes have occurred.

What happened near the fault edges? There are four possible hypotheses (1–4) for the observations concerning the fault edges:

(1) The stress field before the mainshock was homogeneous, and the strength along the edge and extension of the fault may have been very large, and in extreme cases, there were no pre-existing planes of weakness in the extension;

(2) the stress field before the earthquake may not have been homogeneous, such that the concentration of stress only occurred in the area of the mainshock slip;

(3) before the earthquake, stress relaxation occurred along the edges and extensions; or

(4) after the earthquake, inelastic deformation may have occurred along the edges and the extension.

Hypothesis (1) corresponds to an ordinary high-strength barrier, as stated above. This is hypothesised, since large earthquakes are inevitably generated at the edge if the strength of the fault is uniform under the assumed homogeneous stress field before the mainshock, as shown in Fig. 1a. However, it is known that in the case of this barrier, aftershocks are concentrated around the fault edges[16,33]. Furthermore, hypothesis (1) is unlikely because, as shown at the depth of 5 km in Fig. 4b, several normal faulting aftershocks occurred, even in the region where there were almost no strike-slip faulting aftershocks despite of the large ΔCFS for the strike-slip fault. Meanwhile, hypothesis (4) is inconsistent with the results of a geodetic study, which showed that post-seismic slip was not detected along the fault edges and extensions, but instead in the co-seismic slip area and in the near-surface shallower region[30].

Aseismic slip along the edges and extensions is a strong candidate that realises hypothesis (2), as shown in Fig. 1b, d, e.

This is an extreme case, in which aseismic slip (A) mainly occurred on the fault shown by grey around the mainshock fault and the magnitude of the slip is the uniform block slip minus the coseismic slip, as shown in Fig. 1d. The stress due to the aseismic slip is shown as a dashed line in Fig. 1b, which is the reverse of the stress change due to the coseismic slip[34]. This would have occurred near the region of strong coupling at the plate boundary[35]. After the earthquake, the stress before the earthquake is cancelled by the coseismic change, then the stress state becomes flat and there is no stress concentration. In this case, no large earthquakes occur at the edge and in the extension. However, this may not have been the case, for the same reason why we rejected hypothesis (4), since an aseismic slip area is generally characterised by post-seismic slip[36]. Furthermore, post-seismic slip is usually accompanied by the migration of aftershocks[37], which was not observed for the Central Tottori earthquake[30].

As the above case is an extreme one, we examined another possible candidate for stress accumulation only near the earthquake fault: the aseismic slip in the ductile fault zone below the seismic belt in the San'in district[25,38]. Nishimura and Takada (2017) explained GNSS velocity data by the aseismic slip below a depth of 16 km shown in Fig. 1e. The magnitude of the aseismic slip is calculated as the magnitude of the accumulated shear stress averaged on the earthquake fault is equal to that of the stress change by the mainshock. The stress states before and after the mainshock are shown in Fig. 1c as the dashed and dotted lines, respectively. Although unlike the case of the uniform stress shown in Fig. 1a, the region where the stress after the mainshock is greater than the strength is limited to the vicinity of the edges, the region is approximately a half of the length of the mainshock fault. In this case, it is unlikely that an earthquake as large as that expected in the case of the uniform stress will occur at the edge and in the extension. However an earthquake of a considerable magnitude, the fault of which is longer than half the mainshock fault, could occur there, and it is thought that the observed results cannot be explained by this model.

Hypothesis (3) corresponds to another barrier[17], as stated above, and is schematically visualised in Fig. 5, in which the mainshock slip is confined by the regions of stress relaxation, by the near-surface layer, and the deeper ductile fault zone. The mainshock fault should have slightly penetrated into these
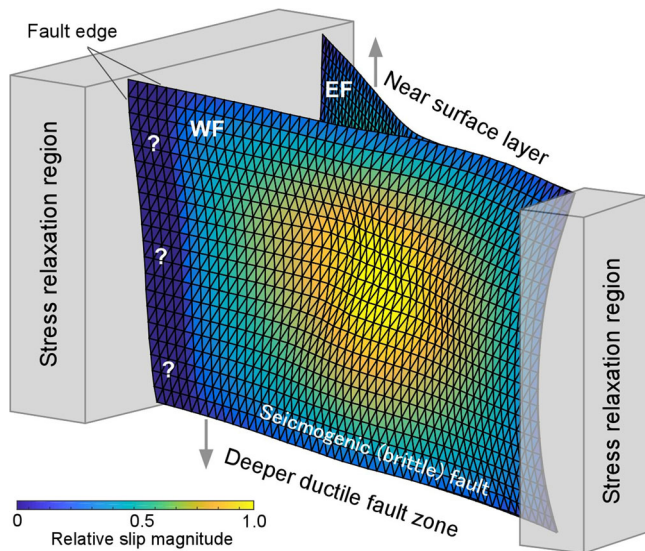
Fig. 5 Estimated fault plane and stress relaxation regions at the horizontal edges and extensions. The fault planes are shown at ~3× magnification in the direction perpendicular to the fault strike. Triangular subfaults used in stress and displacement calculations are shown with the assumed slip distribution, which increases from blue to yellow coloured subfaults. For the WF, the case of the northern edge of $Y = 6.1$ km is shown; however, this value was not well estimated and is possibly located at either location in the portion shown by dark blue. The fault planes are also bounded by the near-surface (inelastic) layer and the deeper ductile fault zone.

regions, but presently, we have no clear evidence for this. In this case, a large earthquake is unlikely to occur in this extension because the shear stress decreased due to stress relaxation. The reason why post-seismic deformation was not detected along the fault edges and extensions may be a large relaxation time due to low temperatures. Additionally, a large earthquake might not occur in the extension of the fault but in a conjugate direction[5], for which the evaluation of the stress state requires further study.

We finally discuss the northern edge. There were few aftershocks along the EF in the northern part, and very few aftershocks occurred along the edge and in the northern extension, as shown in Fig. 3 and Supplementary Fig. 2. This is in harmony with the results in the southern part. Concerning the WF, the northern edge was not well determined and estimated to be at $Y = 6.1−6.9$ km, based on focal mechanism data (see "Methods", Supplementary Fig. 12). If the edge was at $Y = 6.9$ km, in one extreme case, this position almost coincides with the limit of the aftershock distribution, as shown in Fig. 3 and Supplementary Fig. 2. As shown in Fig. 2, a quaternary volcano is located near this northern edge[39]. In the case of the other extreme, $Y = 6.1$ km, as shown at the depths of 5–6 km (Supplementary Fig. 6b), there were also few earthquakes in the region where the ΔCFS for the strike-slip faulting aftershocks were larger. However, this tendency is less remarkable than that around the southern edge, possibly because another minor fault other than the WF and EF may exist due to branching or horsetail structures[22].

Since we were able to precisely determine the positions of an earthquake fault and its horizontal edges, by utilising a large number of well-determined focal mechanism solutions obtained from the rapidly deployed high-density seismic network[24], we believe that our results are reliable. However, only one moderate earthquake was studied and whether or not the observed trends are common to other earthquakes is an important issue requiring

further study. A similar pattern of the P axis azimuth was recognised around the southern edge of the 2000 Western Tottori earthquake (Mw6.6), and it was estimated that the deviatoric stress in the $2 × 2$ km^2 area around the edge was as small as 5 MPa at a depth of 7 km[29]. Moreover, according to the results of seismic velocity tomography in the San'in district, including aftershock regions of moderate to large earthquakes, low-velocity anomalies were systematically estimated to be located near both ends of the aftershock regions[40,41]. These results suggest that stress relaxation at the fault edge may be a common phenomenon for large intraplate earthquakes that are not followed by larger earthquakes.

Methods

Aftershock locations. We only used manually picked data from stations within 50 km of the epicentre. We located hypocentres using the hypomh_ps programme[25], assuming a one-dimensional velocity structure, estimated in the aftershock area of the 2000 Western Tottori Prefecture earthquake[42], which was adjacent to the current study area. In the hypomh_ps programme, the origin time was eliminated from the location problem. Thus, we could estimate reliable hypocentres without a trade-off between the origin time and hypocentre[43,44]. We first determined hypocentres without station corrections. Then, we calculated the averages of the observed minus calculated (O − C) values for the P- and S-waves at each station for earthquakes that had ≥ 30 manually picked P-wave arrival time data points and used them as station correction information. While calculating the averages of the O − C values, values > 0.5 s for P-waves and > 1.5 s for S-waves were omitted. Most errors in the hypocentre calculation were 30–40 m in the horizontal direction and approximately twice that in the vertical direction. For more details, we refer to Iio et al.[24]. We confirmed that the estimated aftershock distribution was very similar to that estimated with tomoDD[45]; however, the distribution was remarkably different from that estimated with the GrowCrust algorithm[46,47], possibly because it allows iterative changes in origin times.

In this study, we analysed aftershocks that occurred from 06:33 Japan Standard Time (JST) on October 22 to December 15 in 2016. Although aftershocks that occurred from 14:07 JST on October 21 (when the mainshock occurred) to 06:33 JST on October 22 (when the temporal network began operating) were not included in our dataset, we confirmed from the unified catalogue of the Japan Meteorological Agency (JMA) that the hypocentral distribution during this period was very similar to that in the subsequent period.

Focal mechanism solutions. Focal mechanisms for aftershocks were determined using a grid search algorithm described in detail by Iio et al.[48]. In this study, we only used focal mechanisms with P-wave polarities of 15 or more, 10 or fewer fault-plane solutions, and an uncertainty of < 60° (estimated from the Kagan angle[49]) between the two most different solutions). The number of focal mechanisms that remained after the above screening process was 10,075, and the average uncertainty of the focal mechanisms was 13.2°. In this study, we selected one optimal fault-plane solution from multiple solutions for each event and analysed the P and T axes of the solution. If all the best solutions for an event had no inconsistent polarities, we selected the solution with the nodal planes that were the farthest from the polarity data on the focal sphere; however, if the best focal mechanisms had inconsistent polarities, we selected a solution with a nodal plane closest to the inconsistent polarities[50]. Examples of focal mechanism solutions are shown in Supplementary Fig. 1. Those for aftershocks around the southern edge in Fig. 3 are shown separately for the eastern and western sides of the fault. Magnitudes ranged from −0.6 to 2.4. Each focal mechanism solution was well-determined, and many normal faulting aftershocks occurred on the eastern side.

Estimation of the true mainshock fault plane—T axis azimuth profiles. It appears that the azimuths of the P and T axes were shifted near the mainshock fault plane at all depths (Fig. 3 and Supplementary Fig. 2). To confirm that these data reflected the stress state in the aftershock area, we performed stress inversion analysis according to the ordinary method, details of which are presented in Iio et al.[48]. We assumed that the stress state was uniform in each sub-region, which was 1 km cuboid, and the length of the sub-region in the X direction was reduced to include focal mechanisms less than 50. Each sub-region overlapped with the adjacent sub-region by half its length. Further, each sub-region was set to exclude the WF, at which clear T axis shifts were observed. As shown in Supplementary Fig. 7, we found that the distributions of the azimuths of the P and T axes were in accordance with those of σ_1 and σ_3, respectively; thus, it is reasonable to explain them based on the changes in stress caused by the mainshock.

Changes in the azimuths of the T axis along the fault-normal direction were investigated for every cuboid region, including the $1 × 1$ km^2 subfault over the entire fault, and the results at a depth of 5 km are shown in Supplementary Fig. 8 (all results are shown in Movie S1). We only used the data with T axis plunges < 30°, and 140° < T axis azimuths < 260°, from −6 to −3 km in the X-direction. On the boundary of the fault, step-wise changes were observed for many of the regions,

with changes showing opposite patterns in the north and south that were consistent with the changes in stress due to the mainshock slip. Assuming that the fault was located at the positions of these steps, we approximated the T axis azimuth data with a step-wise function (tanh(aX)) and attempted to detect the three-dimensional positions of the fault using a nonlinear least-squares method. The value of parameter a of the stepwise function was set as 20, considering errors in hypocentre locations. We weighted the data such that it was inversely proportional to the error of focal mechanism solutions measured by the Kagan angle[49], as shown in Supplementary Fig. 8. The minimum error was set as 4°. Initial values were set by a grid search. Fault positions were estimated at grids at the centre of each subfault and the grids were distributed as each subfault overlapped the adjacent one by half its length. When data were not fitted well, results of the initial grid search are shown, but 95% confidence intervals (CIs) of estimated fault positions and T axis azimuths are not shown. For many grids, the estimated fault positions are different from ordinary estimations that were obtained by minimising the sum of the squared distance between the fault positions and aftershock hypocentres[28], beyond the 95% CIs, suggesting that it may not be possible to accurately estimate the mainshock fault plane only from aftershock hypocentre data.

Estimation of the true mainshock fault plane—single fault model. We only used data estimated at the grids where the 95% CIs of T axis azimuths on both sides of the fault did not overlap, the AIC was significant when compared to the model without the step, the amount of data on one side of the estimated fault was ≥ 5, Z > −11 km, and −3 km < Y < 7 km; the last condition was used to exclude data far from the expected mainshock fault plane. From these data, we estimated the mainshock fault plane by local linear approximation using the 'fit' function in MATLAB v.9.3.0 (MathWorks, USA) with the "lowess" (locally weighted scatter plot smooth) option. We used fault position data weighted inversely proportional to the 95% CIs and set a parameter for the extent of data used by the local regression to be 0.1, which corresponded to a cut-off length of ~2 km, that is, twice the subfault length. If smaller values for this parameter had been used, a bumpy fault plane would have been estimated. The estimated fault plane is shown in Supplementary Fig. 9, along with the data used. The data are also shown in Supplementary Fig. 3b with the distributions of T axes. In this approximation, finer grids were estimated at the intervals of ~200 m in the fault strike direction and ~500 m in the dip direction, for subsequent calculations of stress. However, it appears that several fault position data are distributed on the eastern side, apart from the estimated fault, in the region of Y > 2 km. Furthermore, we found that slip on the estimated fault cannot fully explain the coseismic displacements deduced from the GNSS measurements shown by red arrows in Supplementary Fig. 10[30].

Estimation of the true mainshock fault plane—two-fault model. Then, we estimated two fault planes from the same dataset obtained above. First, we estimated the WF by using the data where X < −4.2 km if Y > 3 km. If Y ≤ 3 km, all the data were used. Next, we set the weights of the fault positions of Y < 2 km estimated in the first step, to 1, namely the fault positions of Y < 2 km were almost fixed, and estimated the EF by using the data where X ≥ −4.2 km if Y > 3 km. The estimated WF and EF are shown in Supplementary Fig. 11. It was found that the data from the eastern side, apart from the single fault, were well fitted by EF.

In these steps, the edges of the fault planes were not determined, since extrapolation was also performed outside the aftershock region. Supplementary Figs. 9 and 11 were drawn considering the results for the fault edges described below.

Estimation of locations of the southern fault edge. Here, we first estimated the southern fault edge. Tensional stress is generally concentrated on one side of the horizontal edges of strike-slip faults. As the regional stress state across the islands of Japan is essentially compressional[51], normal faulting earthquakes are the most likely to occur in regions where tensional stress is concentrated. Thus, it can be expected that the horizontal edges of the mainshock fault of the Central Tottori earthquake would be located where the ΔCFS for normal faulting aftershocks was maximised. In the calculation of ΔCFS, **μ** was set to 0.4, following previous aftershock studies[6]. We then assumed several fault models with fault edges in different locations, and calculated ΔCFS for normal faulting aftershocks with a P-axis plunge > 60°. For simplicity, horizontal edges were not allowed to vary with depth. The upper and lower edges were set to depths of 1.6 and 11.8 km, respectively, following the aftershock distribution. The distributions of slip magnitudes were assumed to be tapered linearly by widths of 4 km from the horizontal, 3.5 km from the upper, and 5 km from the lower edges of the fault, following the fault model with varying slip magnitudes estimated from InSAR and GNSS data[30]. Here, we did not refer to the fault slip models estimated from strong-motion data[32,46], because these models cannot explain the coseismic displacements[30]. We confirmed that the minor changes in the slip distribution, such as different taper lengths, rarely affect the results. The absolute amount of slip was normalised so that the seismic moment matched that determined by the fault model[30].

We calculated the contribution from all of the triangular subfaults obtained by the Delaunay separation of the grid data of the curved fault plane estimated above using the Meade programme[52], to solve the problem of singularities[53] by shifting

points to calculate. The distributions of ΔCFS for normal faulting aftershocks are shown in Supplementary Fig. 3 for different positions of the southern fault edge. The moment ratio of the western and eastern faults was assumed to be 0.4:0.6, and both northern edges were set at Y = 6.1 km, which did not affect the following result. Aftershocks within 100 m from the fault plane were excluded, because errors in hypocentres for those events could cause substantial adverse effects. The ΔCFS values were computed for both the nodal planes and larger values were adopted. We averaged ΔCFS within a cuboid area with a height of 13 km and a horizontal cross-section of 2 km², centred on assumed fault edges. The relationship between the mean ΔCFS and the positions of horizontal fault edges is shown in Supplementary Fig. 12a. The position of the southern edge was well-estimated as the position that maximises the mean ΔCFS value (Y = −2.6 km). This is within 1σ CIs of those of the uniform slip model[54].

Estimation of locations of the northern fault edges. To estimate the locations of the northern fault edges, we utilised the coseismic displacements deduced from the GNSS measurements[30] (which are shown by red arrows in Supplementary Fig. 10), because few aftershocks occurred around the northern edge of the EF, as seen in Fig. 3 and Supplementary Fig. 2, and several GNSS stations are located near the northern edges (Supplementary Fig. 10). We assumed several variations for the locations of both the fault edges and the moment ratio of the WF and EF and calculated the differences between the observed and calculated coseismic displacement vectors. For simplicity, the locations of the horizontal edges were not allowed to vary with depth. As in the previous section, the distributions of slip magnitudes were assumed to be tapered linearly by widths of 4 km from the horizontal, 3.5 km from the upper, and 5 km from the lower edges, for both the faults.

The results are shown in Supplementary Fig. 13. We assumed the locations of the northern fault edge of the WF from 5.7 to 7.3 km in 0.2 km steps. We calculated the RMS misfits (mm) between the observed and calculated vectors for locations of the northern fault edge of the EF from 5.7 to 7.3 km in steps of 0.2 km and the moment ratios of the WF from 0 to 1 in steps of 0.2. For many cases of the WF, the minimum value was obtained for the location of the northern fault edge of the EF of 6.1 km and the moment ratios of the WF of 0.4. A ratio of 0 or 1 meant only the EF or WF, respectively, and misfits were exceptionally large in these cases. Using these values, changes in the misfits are shown for different locations of the northern fault edge of the WF in Supplementary Fig. 12c. A broad minimum with a gentle peak was observed around Y = 6.5 km.

By the same method used in the previous section, we estimated the location of the northern fault edge of the WF from focal mechanism data. However, as shown in Supplementary Fig. S12b, a broad peak can be observed from Y = 6.1 to 6.9 km, and the northern edge could not be clearly determined using the focal mechanism data or the GNSS data.

The estimated faults are compared with P and T axes, and stress states in Supplementary Figs. 2 and 7, respectively. The extent of the estimated northern edges of the WF is indicated by pink and blue dashed lines from Y = 6.1 to 6.9 km in Supplementary Figs. 2 and 7, respectively. In the case of Y = 6.9 km, it can be observed that the northern edge is located at the northern end of the aftershock distribution, and that very few aftershocks occur north of the edge in Supplementary Fig. 2. It appears that in this case, the WF almost penetrates the aftershock distribution. However, in Fig. 3 and Supplementary Fig. 6, we used the northern edge of Y = 6.1 km and calculated the stress field as the opposite extreme case. This is because, in the case of the northern edge of Y = 6.9 km, it is not effective to show ΔCFS around the edge, due to the absence of aftershocks north of the edge. The estimated fault models with the distributions of slips are shown in Fig. 4. In the southern part, the WF and EF are unified because of the same geometries.

Calculation of shear stress on a simple planar vertical strike-slip fault and in the extension. To evaluate the stress concentration near the horizontal edges of a mainshock fault, we assumed a simpler fault slip model and calculated the stress state after the mainshock in Fig. 1. We assumed that the fault plane was a simple planar vertical strike-slip fault with the same horizontal and lower edges as the EF. For simplicity, the upper edge was set at the surface and the slip distribution was assumed to be uniform in the vertical direction. This implicitly assumes that postseismic deformation occurs near the surface as was partly observed by the GNSS and InSAR measurements[30]. The slip distribution was tapered horizontally by the square root taper of the width of 4 km, to evaluate the stress state near the horizontal edges. The average stress drop on the mainshock fault was computed to be 3.4 MPa. The shear stresses on the fault and extension due to the slip distributions were calculated at depths of 5 km along the fault strike on a plane 100 m orthogonal to the fault by the programme of Nikkhoo and Walter (2015)[53]. We assumed a Poisson's ratio of 0.25 and a rigidity of 35 GPa. The reason for calculating this on a plane 100 m orthogonal to the fault was practically to avoid singularities on faults and the stress concentration at points very close to the fault edge.

Data availability

References

1. Madariaga, R. High-frequency radiation from crack (stress drop) models of earthquake faulting. *Geophys. J. Int.* **51**, 625–651 (1977).
2. Rubin, A. M. Aftershocks of microearthquakes as probes of the mechanics of rupture. *J. Geophys. Res.* **107**, ESE-3 (2002).
3. Gulia, L. & Wiemer, S. Real-time discrimination of earthquake foreshocks and aftershocks. *Nature* **574**, 193–199 (2019).
4. Mancini, S., Segou, M., Werner, M. J. & Cattania, C. Improving physics-based aftershock forecasts during the 2016–2017 Central Italy Earthquake Cascade. *J. Geophys. Res.* **124**, 8626–8643 (2019).
5. Ross, Z. E. et al. Hierarchical interlocked orthogonal faulting in the 2019 Ridgecrest earthquake sequence. *Science* **366**, 346–351 (2019).
6. Stein, R. S., King, G. C. P., Lin, J. & Palm, N. Change in failure stress on the southern San Andreas fault system caused by the 1992 magnitude = 7.4 Landers earthquake. *Science* **258**, 1328–1332 (1992).
7. Hardebeck, J. L., Nazareth, J. J. & Hauksson, E. The static stress change triggering model: constraints from two southern California aftershock sequences. *J. Geophys. Res.* **103**, 24427–24437 (1998).
8. DeVries, P. M. R. et al. Deep learning of aftershock patterns following large earthquakes. *Nature* **560**, 632–634 (2018).
9. Kilb, D., Gomberg, J. & Bodin, P. Triggering of earthquake aftershocks by dynamic stresses. *Nature* **408**, 570–574 (2000).
10. Felzer, K. R. & Brodsky, E. E. Testing the stress shadow hypothesis. *J. Geophys. Res.* **110**, B05S09 (2005).
11. Brodsky, E. E. & Van der Elst, N. J. The uses of dynamic earthquake triggering. *Annu. Rev. Earth Planet. Sci.* **42**, 317–339 (2014).
12. Miller, S. A. et al. Aftershocks driven by a high-pressure CO2 source at depth. *Nature* **427**, 724–727 (2004).
13. Reasenberg, P. A. & Jones, L. M. California aftershock hazard forecast. *Science* **243**, 1173 (1989).
14. Ide, S. Frequent observations of identical onsets of large and small earthquakes. *Nature* **573**, 112–116 (2019).
15. Ellsworth, W. L. & Beroza, G. C. Seismic evidence for an earthquake nucleation phase. *Science* **268**, 851–855 (1995).
16. Aki, K. Characterization of barriers on an earthquake fault. *J. Geophys. Res.* **84**, 6140–6148 (1979).
17. Yue, H. et al. The 2016 Kumamoto Mw = 7.0 earthquake: A significant event in a fault–volcano system. *J. Geophys. Res.* **122**, 9166–9183 (2017).
18. Galis, M., Ampuero, J. P., Mai, P. M. & Cappa, F. Induced seismicity provides insight into why earthquake ruptures stop. *Sci. Adv.* **3**, eaap7528 (2017).
19. Ke, C. Y., McLaskey, G. C. & Kammer, D. S. The earthquake arrest zone. *Geophys. J. Int.* **224**, 581–589 (2021).
20. King, G. C. P. & Nabelek, J. F. Role of fault bends in the initiation and termination of earthquake rupture. *Science* **228**, 984–987 (1985).
21. Sibson, R. H. Stopping of earthquake ruptures at dilational fault jogs. *Nature* **316**, 248–251 (1985).
22. Young-Seog, K. & Sanderson, D. J. Structural similarity and variety at the tips in a wide range of strike-slip faults: a review. *Terra Nova* **18.5**, 330–344 (2006).
23. Wesnousky, S. Predicting the endpoints of earthquake ruptures. *Nature* **444**, 358–360 (2006).
24. Iio, Y. et al. Stationarity of aftershock activities of the 2016 Central Tottori Prefecture earthquake revealed by dense seismic observation. *EPS* https://doi.org/10.1186/s40623-020-01161-x (2020).
25. Kawanishi, R., Iio, Y., Yukutake, Y., Shibutani, T. & Katao, H. Local stress concentration in the seismic belt along the Japan Sea coast inferred from precise focal mechanisms: implications for the stress accumulation process on intraplate earthquake faults. *J. Geophys. Res.* **114**, B01309 (2009).
26. Earthquake Research Committee. *Evaluation of Earthquake Central Tottori Prefecture on October 21, 2016.* (last accessed 2 May 2021); https://www.static.jishin.go.jp/resource/monthly/2016/20161021_tottori.pdf.
27. Liu, J., Sieh, K. & Hauksson, E. A structural interpretation of the aftershock "Cloud" of the 1992 Mw 7.3 Landers earthquake. *Bull. Seismol. Soc. Am.* **93**, 1333–1344 (2003).
28. Yukutake, Y. & Iio, Y. Why do aftershocks occur? Relationship between mainshock rupture and aftershock sequence based on highly resolved hypocenter and focal mechanism distributions. *EPS* https://doi.org/10.1186/s40623-017-0650-2 (2017).
29. Yukutake, Y., Iio, Y., Katao, H. & Shibutani, T. Estimation of the stress field in the region of the 2000 Western Tottori Earthquake: using numerous aftershock focal mechanisms. *J. Geophys. Res.* **112**, B09306 (2007).
30. Meneses-Gutierrez, A., Nishimura, T. & Hashimoto, M. Coseismic and postseismic deformation of the 2016 Central Tottori earthquake and its slip model. *J. Geophys. Res.* **124**, 2202–2217 (2019).
31. Gahalaut, K. & Gahalaut, V. K. Stress triggering of normal aftershocks due to strike slip earthquakes in compressive regime. *J. Asian Earth Sci.* **33**, 379–382 (2008).
32. Kubo, H., Suzuki, W., Aoi, S. & Sekiguchi, H. Source rupture process of the 2016 Central Tottori, Japan, earthquake (M JMA 6.6) inferred from strong motion waveforms. *Earth Planets Space* **69**, 127 (2017).
33. Sibson, R. H. Earthquake faulting as a structural process. *J. Struct. Geol.* **11**, 1–14 (1989).
34. Savage, J. C. & Burford, R. O. Geodetic determination of relative plate motion in central California. *J Geophys Res.* **78**, 832–845 (1973).
35. Kanamori, H. In *Island Arcs, Deep Sea Trenches and Back-Arc Basins* 163–174 (American Geophysical Union, 1977).
36. Marone, C., Scholz, C. & Bilham, R. On the mechanics of earthquake afterslip. *J. Geophys. Res.* **96**, 8441–8452 (1991).
37. Wesson, R. L. Modelling aftershock migration and afterslip of the San Juan Bautista, 1125 California, earthquake of October 3, 1972. *Tectonophysics* **144**, 215–229 (1987).
38. Nishimura, T. & Takada, Y. San-in shear zone in southwest Japan revealed by GNSS observations. *Earth, Planets Space* **69**, 85 (2017).
39. Geological Survey of Japan. *Quaternary Volcanoes of Japan 2021* (last accessed 02 May 2021); https://gbank.gsj.jp/volcano/Quat_Vol/index_e.html
40. Coordinating Committee of Earthquake and Volcanic Eruption Prediction Researches. *2012 Annual Report of Observation Research Plan for Predicting Earthquakes and Volcanic Eruptions (2-1) Earthquake preparation process* (last accessed 12 November 2020) (2013); https://www.mext.go.jp/component/b_menu/shingi/toushin/__icsFiles/afieldfile/2013/12/06/1341717_03.pdf
41. Suemoto, Y., Ikeda, T., Tsuji, T. & Iio, Y. Identification of a nascent tectonic boundary in the San-in area, southwest Japan, using a 3D S-wave velocity structure obtained by ambient noise surface wave tomography. *Earth, Planets Space* **72**, 1–13 (2020).
42. Shibutani, T. et al. High resolution 3-D velocity structure in the source region of the 2000 Western Tottori Earthquake in southwestern Honshu, Japan using very dense aftershock observations. *Earth Planets Space* **57**, 825–838 (2005).
43. Matsu'ura, M. Bayesian estimation of hypocentre with origin time eliminated. *J. Phys. Earth* **32**, 469–483 (1984).
44. Hirata, N. & Matsu'ura, M. Maximum-likelihood estimation of hypocentre with original time eliminated using nonlinear inversion technique. *Phys. Earth Planet. Interior* **47**, 50–61 (1987).
45. Zhang, H. & Thurber, C. H. Double difference tomography: The method and its application to the Hayward fault. *California. Bull. Seismol. Soc. Am.* **93**, 1889 (2003).
46. Ross, Z. E., Kanamori, H., Hauksson, E. & Aso, N. Dissipative intraplate faulting during the 2016 Mw 6.2 Tottori, Japan earthquake. *J. Geophys. Res.* **123**, 1631–1642 (2018).
47. Trugman, D. T. & Shearer, P. M. A hierarchical clustering algorithm for relative earthquake relocation, With application to the Spanish Springs and Sheldon, Nevada, earthquake sequences. *Seismol. Res. Lett.* **88**, 379–391 (2017).
48. Iio, Y. et al. Which is heterogeneous, stress or strength? An estimation from high-density seismic observations. *EPS* **69**, 144 (2017).
49. Kagan, Y. Y. 3-D rotation of double-couple earthquake sources. *Geophys. J. Int.* **106**, 709–716 (1991).
50. Maeda, N. A method of determining focal mechanisms and quantifying the uncertainty of the determined focal mechanisms for microearthquakes. *Bull. Seismol. Soc. Am.* **82**, 2410–2429 (1992).
51. Oike, K. & Huzita, K. Relation between characteristics of seismic activity and neotectonics in Honshu, Japan. *Tectonophysics* **148**, 115–130 (1988).
52. Meade, B. J. Algorithms for the calculation of exact displacements, strains, and stresses for triangular dislocation elements in a uniform elastic half space. *Comput. Geosci.* **33**, 1064–1075 (2007).
53. Nikkhoo, M. & Walter, T. R. Triangular dislocation: an analytical, artefact-free solution. *Geophys. J. Int.* **201**, 1119–1141 (2015).
54. Geospatial Information Authority of Japan. *Source Fault Model of Central Tottori Earthquake (Rectangular Fault Model with Uniform Slip) 2017* (last accessed 12 November 2020); https://www.gsi.go.jp/common/000147191.pdf

Author contributions

Y.I. carried out the data analysis. S.M. and Y.Y. designed and implemented the observation plan. S.S., T.Iwasaki., H.K. and A.K. supervised the data acquisitions. M.S. carried out the data processing. K.T., T.I., M.K., E.K., Y.T., H.T. and T.U. carried out the data acquisition. All authors read and approved the paper.

Competing interests

The authors declare no competing interests.

Additional information

Supplementary information The online version contains supplementary material available at https://doi.org/10.1038/s43247-021-00231-6.

Correspondence and requests for materials should be addressed to Y.I.

Peer review information *Communications Earth & Environment* thanks Jean-Paul Ampuero and the other, anonymous, reviewer(s) for their contribution to the peer review of this work. Primary Handling Editors: Luca Dal Zilio, Joe Aslin, Heike Langenberg. Peer reviewer reports are available.

Reprints and permission information is available at http://www.nature.com/reprints

Publisher's note Springer Nature remains neutral with regard to jurisdictional claims in published maps and institutional affiliations.